Determination of the charge ordered phases in $LuFe_2O_4$

Sara Lafuerza,[1,2] Gloria Subías,[2] Javier Blasco,[2] Joaquín García,[2*] Gareth Nisbet,[3] Kazimierz Conder[4] and Ekaterina Pomjakushina.[4]

[1]ESRF-The European Synchrotron, CS40220, F-38043 Grenoble Cedex 9, France

[2]Instituto de Ciencia de Materiales de Aragón (ICMA), CSIC-Universidad de Zaragoza, Departamento de Física de la Materia Condensada, Pedro Cerbuna 12, 50009 Zaragoza, Spain

[3]Diamond *Light Source* Ltd., Diamond House, Harwell Science and Innovation Campus, Didcot, Oxfordshire OX11 0DE, United Kingdom

[4]Laboratory for Developments and Methods, Paul Scherrer Institut, 5232 Villigen PSI, Switzerland

PACS numbers:75.47.Lx; 61.05.C-;75.25.Dk

*E-mail: jgr@unizar.

Abstract

High resolution synchrotron powder diffraction (HRPD) and Fe K-edge x-ray resonant scattering (RXS) have been combined to determine both the magnitude and sequence of the Fe charge segregation in $LuFe_2O_4$. Two phases with different charge disproportionation were found below the so-called charge ordering (CO) transition temperature $T_{CO}\approx$320 K. The crystal structure between 320 K and 200 K shows a *C2/m* symmetry where four non-equivalent iron sites with different valences were determined ($Fe^{2.77+}$, $Fe^{2.63+}$ $Fe^{2.36+}$ and $Fe^{2.26+}$). Below 200 K the structure further changes to the *P-1* symmetry and six crystallographic sites for the iron atoms were found. The simplest valence distribution corresponds to a tri-modal one, where the six Fe atoms are grouped in couples with three valences $Fe^{2.8+}$, $Fe^{2.5+}$ and $Fe^{2.2+}$. Both polar and anti-polar charge sequences have been discarded.

Multiferroic oxides that bring together ferroelectric and ferromagnetic orderings with added strong magnetoelectric coupling have drawn enormous attention in the last decades [1]. Regrettably, multiferroic materials are scarce since the conventional origin of ferroelectricity (FE) is incompatible with magnetism [2]. Charge ordering (CO) has been recently proposed as a new route leading to the appearance of FE [3]. Nonetheless, examples of oxides showing this type of FE are limited and the origin of the electrical polarization in terms of the valence ordering is not well understood. The main weakness lies in the question of whether CO really occurs in mixed valence oxides. Indeed, most of the recent studies of CO phases in mixed valence oxides have challenged the occurrence of an ordering of ionic valence states. The resulting CO phases imply either a multimodal valence distribution, where the maximum charge disproportion is a small fraction of one electron [4,5], or a continuous sinusoidal modulation, *i.e.* a charge-density-wave [6].

$LuFe_2O_4$ has been considered as the prototypical example of CO-based ferroelectricity [3] derived from both macroscopic electric properties measurements by dielectric spectroscopy and pyroelectric current detection and on a credible microscopic model of polar CO [7]. According to this model, Fe valence ordering has been suggested to render the triangular Fe-O bilayers polar by making one of the two layers rich in Fe^{2+} and the other in Fe^{3+} [7]. Due to the novel mechanism for FE and also because of the high transition temperatures of CO ($T_{CO}\approx$320 K) and magnetic ordering ($T_N\approx$240 K), this compound has been matter of extensive study [7–16]. However, a detailed characterization of the intrinsic dielectric properties has recently shown that $LuFe_2O_4$ is not ferroelectric [17-19]. The reported large dielectric constants correspond solely to extrinsic effects originated from the electrodes, *e.g.* due to the Schottky-type depletion layers at the contact interfaces [16-18] and $P(E)$ loops measured at low temperatures (10 K) and electric fields of about 30 kV/cm do not show spontaneous electrical polarization [19]. At the same time, a single crystal x-ray diffraction study by J. de Groot *et al.* [20] has proposed a monoclinic structure for the CO phase that implies a stacking of non-polar Fe bilayers oppositely charged along the *c*-axis (*i.e.* anti-polar ordering). Although this refinement contains four Fe-sites with valences determined by bond-valence-sum (BVS) method [21] they are grouped into a bimodal valence distribution, 2.04 and 2.80 [20], which are considered to be remarkably close to the

integer valences +2 and +3 and thus still support the ionic picture of $Fe^{2+/3+}$ CO in $LuFe_2O_4$.

Further support for the CO picture in $LuFe_2O_4$ came from the x-ray resonant scattering technique [7,22,23]. Superstructure reflections at positions (1/3, 1/3, *half-integer*) of the hexagonal cell showing characteristic resonances at the Fe K-edge were observed by several groups. However, we note that these studies only performed a qualitative analysis of the resonant scattered intensity without considering the low-temperature structure factor and the CO sequence. On the other hand, x-ray absorption spectroscopy at the Fe K-edge discards the total ionic Fe^{2+}/Fe^{3+} segregation and establishes the maximum charge disproportionation among the different Fe sites in the lattice to be 0.5 electrons [24].

In this letter, we present a complete study of the crystal structure and both the magnitude and sequence of the Fe charge segregation below T_{CO} in $LuFe_2O_4$ by means of high resolution synchrotron powder diffraction (HRPD) and x-ray resonant scattering (RXS) at the Fe K-edge in an oriented single crystal. Two different superstructures associated with the condensation of various soft phonon modes have been found upon cooling below T_{CO}. All the superstructure reflections are indexed in the hexagonal setup. The first structural transition at $T_{CO}\approx$320 K from hexagonal $R\bar{3}m$ to monoclinic *C2/m* is mainly driven by modes of symmetry Y_2 that give rise to the (1/3, 1/3, *l*/2) *l*=odd reflections. The associated distortions imply the distinction of four non-equivalent Fe sites but a four-modal valence distribution instead of the almost bimodal one reported in [20] is found. This results in equally charged (+2.44) and non-polar Fe bilayers as opposed to the anti-polar ordering deduced in [20]. Below T_N, we find a second crystal symmetry change from monoclinic *C2/m* to triclinic $P\bar{1}$. The prevailing oxygen distortion giving rise to the triclinic structure is mainly driven by modes of the irreducible representation (Irrep) Γ_2^+ and results in an additional charge disproportionation between the monoclinic Fe sites at Wyckoff positions *8j*. This triclinic $P\bar{1}$ low-temperature structure explains the appearance of resonant (1/3, 1/3, *l*) *l*=integer reflections and the most simple Fe valence distribution is found to be trimodal.

The polycrystalline and single crystal samples of $LuFe_2O_4$ are the same as those employed in previous studies [19, 24], showing the expected CO transition at 320 K and ferrimagnetic ordering at 240 K. HRPD patterns were collected between 80 K and 400 K at beamline ID31 [25] of the ESRF synchrotron (Grenoble, France) with a short

wavelength λ = 0.3542 Å in order to minimize absorption. The structural phase transitions were first analysed in terms of a symmetry-mode decomposition using the ISODISPLACE [26] and AMPLIMODES [27] tools. Finally, diffraction patterns were refined by the Rietveld method using the FULLPROF package [28]. RXS experiments at the Fe K-edge were carried out at the Diamond Light Source (Oxford, UK) at beam line I16 [29] on a $LuFe_2O_4$ single crystal (4x3x2 mm) cut and polished with the [*001*] direction as the surface normal. We have detected superlattice reflections correspondent to the three possible monoclinic domains (twinned sample). The energy, polarization (σ-σ' and σ-π' channels were recorded using a MgO (220) crystal analyzer) and temperature (17 to 400 K) dependence of the (1/3, 1/3, *l*/2) *l*=odd; (1/3, 1/3, *l*) *l*=integer and (0, 0, *l*/2) *l*=odd superstructure reflections was investigated by recording their intensities using an avalanche photodiode.

The HRPD pattern of $LuFe_2O_4$ above $T_{CO}\approx320$ K agrees with the expected hexagonal structure (space group $R\bar{3}m$) previously determined [30]. Below T_{CO}, two different phases are distinguished: phase I (320 K > T ≥ 200 K) and phase II (200 K > T ≥ 80 K). Diffraction patterns of phase I show the splitting of some of the main hexagonal diffraction lines and the appearing of (1/3, 1/3, *l*/2) superlattice peaks (see Fig. 1(a)). These changes and the systematic extinctions of reflections (*h, k, l*) with *h+k=odd* are compatible with a C-centered monoclinic cell. In phase II new splittings are observed (see Fig. 1(b)) that can only be accounted for by a triclinic cell. We have explored the possible atomic displacements patterns compatible with Irreps of the parent space-group symmetry able to give the mentioned monoclinic and triclinic cells. First, we have used the high temperature hexagonal structure as the parent symmetry to search among the different solutions of C-centered monoclinic cells. Discarding the non-centrosymmetric solutions (*Cm*, *C2*), which is justified by the proven absence of ferroelectricity [19], the best refinement is obtained for the monoclinic cell with space group *C2/m* and origin (2, 2, -1/2) with respect to the hexagonal cell, which is consistent with the previous single crystal x-ray diffraction study [20]. The structural transition from $R\bar{3}m$ to *C2/m* was found to be driven by the condensation of modes belonging to the Irrep Y_2 (responsible for the appearing of the (1/3, 1/3, *l*/2) reflections) and two set of secondary modes belonging to Irrep Γ_1^+ and Γ_3^+. The main structural parameters for the best refinements are given in table I. There are four non-equivalent Fe sites in the *C2/m* cell whose corresponding valences deduced from BVS analysis are 2.69(3),

2.54(2), 2.29(1) and 2.19(2) for Fe1(*4i*), Fe2(*8j*), Fe3(*8j*) and Fe4(*4i*) respectively, in agreement with a four-modal Fe valence distribution and a charge disproportionation ≤ 0.5 electrons. The significantly smaller charge disproportionation among the different Fe sites as compared with the previous single crystal diffraction study [20] agrees reasonably with results from x-ray absorption spectroscopy [24]. Besides, another major difference with the mentioned structural determination is the lack of differently charged Fe bilayers along the *c*-axis in our *C2/m* cell. This result discards charge modulation along the *z*-direction derived from [20] and is consistent with the absence of resonant behaviour for the (0, 0, *l*/2) *l*=odd superstructure reflections obtained in our RXS measurements as discussed later. Since one bilayer is composed by the pair Fe1-Fe3 and the other with the Fe2-Fe4, the lack of charge modulation between bilayers discards a bimodal distribution (Fe1-Fe2) and Fe3-Fe4 pairs as proposed in [20]. Regarding the symmetry analysis of the phase II, the monoclinic *C2/m* cell has been used as the parent structure and we have retained as the most plausible solution a triclinic structure with space group $P\bar{1}$ and half the volume of the *C2/m* cell. The active modes in the C2/m → $P\bar{1}$ transition belong to the Irreps Γ_1^+ and Γ_2^+ A nice refinement can be obtained by only fitting the cell parameters of the triclinic $P\bar{1}$ cell and the Γ_1^+ modes (see table I). This is equivalent to refine the triclinic cell with the constraints of the monoclinic symmetry and indicates that the atomic displacements specific to the triclinic distortion (Γ_2^+ modes) are very subtle and within the accuracy limit of the x-ray diffraction technique. In order to get a reliable final solution for the triclinic cell, we must take into account the RXS results within this temperature range presented soon after in this letter. Those results imply an additional disproportionation of the monoclinic Fe2 and Fe3 atoms at the *8j* sites into two non-equivalent (2*i*) sites in the triclinic cell. We found that this second charge disproportionation is mostly driven by a particular set of Γ_2^+ modes acting on the oxygen atoms surrounding Fe2 and Fe3 atoms. These modes imply atomic displacements in the ab-plane, ($-\delta_x$, δ_x, 0) and the BVS analysis of the best fit with the addition of only this set of Γ_2^+ modes yielded the following six-modal Fe valence distribution in the $P\bar{1}$ cell: 2.78(1), 2.73(2), 2.39(2), 2.13(1), 2.50(2) and 2.25(1) for Fe1, Fe21, Fe22, Fe31, Fe32 and Fe4 respectively, where the labels are maintained from the monoclinic structure. It is noteworthy that the absence of differently charged bilayers and the small charge disproportionation are maintained in the triclinic cell.

Superlattice (1/3, 1/3, *l*/2) *l*=odd; (1/3, 1/3, *l*) *l*=integer and (0, 0, *l*/2) *l*=odd reflections were investigated by means of RXS across the Fe K-edge. The temperature dependence of the first two types of reflections is given in Fig. 2. On cooling down, reflections with periodicity (1/3, 1/3, *l*/2) *l*=odd appear at $T \leq T_{CO} \approx 320$ K while the (1/3, 1/3, *l*) *l*= integer satellites come out approximately below $T_N \approx 240$ K coincident with the magnetic ordering. This behaviour indicates the occurrence of two successive orderings in consistency with the presence of the two low temperature phases I and II determined by HRPD. The intensity of the (1/3, 1/3, *l*/2) reflections decreases below 240 K when the (1/3, 1/3, *l*) reflections appear indicating a relationship between the two types of orderings. We note a discrepancy between the temperature for the occurrence of (1/3, 1/3, *l*) reflections in the single crystal (~240 K) and the *C2/m* to $P\bar{1}$ transition temperature (~200 K) found in the powder sample. This variance may be due to tiny differences in composition between the specimens. The same applies to the small differences between our temperature evolution of the (1/3, 1/3, *l*/2) reflections and the one reported in ref. [23] for (1/3, 1/3, 7/2).

Both kinds of satellite reflections (1/3, 1/3, *l*/2) and (1/3, 1/3, *l*), show significant Thomson contributions and consequently a strong self-absorption is observed in the energy dependent spectra. This fact suggests a predominant structural character of the phase transitions. On the other hand reflections (0, 0, *l*/2) with *l*=9,15 were also detected but their spectral shape does not show any resonance, their intensity being about two orders of magnitude lower than that of the other two types of reflections and almost constant in the whole temperature range studied up to 400 K. This finding indicates the lack of charge modulation with propagation vector *k*= (0, 0, *l*/2), which agrees with the absence of charge scattering for the (0, 0, 3/2) reflection as reported at the Fe $L_{2,3}$-edges [16] and also concurs with the lack of charge difference between consecutive Fe-bilayers as previously mentioned. For the measured reflections, the energy dependent RXS only shows intensity in the σ-σ' channel and no azimuthal dependence was observed. Figure 3 shows the energy dependent resonant diffracted intensity after self-absorption correction for representative (1/3, 1/3, *l*/2) and (1/3, 1/3, *l*) reflections. The spectral shape of the (1/3, 1/3, *l*/2) reflections agrees with previously published data [7,22,23]. The energy dependence of the scattered intensity is very similar for both types of reflections with strong either cusp or valley resonances at the Fe absorption threshold depending on the *l*/2 and *l* values.

Resonances at the absorption edge come from differences in the anomalous atomic scattering factor (AASF). Since there is no azimuthal dependence of the scattered intensity, the AASF is reduced to a scalar and the structure factor can be expressed by $F_{hkl} = \Sigma_i [f_{0i} + f'_i(E) + i f''_i(E)] \exp(hx_i + ky_i + lz_i)$ where f_{0i} is the Thomson term and f'_i(E) and f''_i(E) are the real and imaginary part of the anomalous term. For the superlattice reflections studied here, in both centrosymmetric *C2/m* and $P\bar{1}$ structures, the energy-independent Thomson term is real and comes from contributions due to displacements of Fe, Lu and/or O atoms while the anomalous term is only due to the non-equivalent crystallographic Fe sites. Since the Thomson scattering term (F_0) is larger than the anomalous part ($F'_{Fe}(E) + iF''_{Fe}(E)$), as shown in fig. 3, we have approximated the intensity of the observed superlattice reflections to: $I_{hkl}(E) \propto |F_{hkl}|^2 \approx (F_0)^2 + 2 \cdot F_0 \cdot F'_{Fe}(E)$. Resonances at energies close to the Fe K-edge occur due to the fact that Fe atoms in the different crystallographic sites of the superlattice exhibit different AASF. The main resonances arise at the absorption edge because of the small differences in its energy position, *i.e.* the chemical shift. The energy position of the absorption threshold is correlated with the formal valence of the atom. Therefore, segregation and ordering of valence states of the different Fe sites can be determined from the quantitative analysis of the energy dependence of the scattered intensity. Let us comment shortly on the limitations of the previously reported RXS analysis [22,23]. As we have stated, for $F_0 >> F'_{Fe}(E) + iF''_{Fe}(E)$ the intensity is well described by the linear interference between F_0 and the real part of the Fe anomalous structure factor $F'_{Fe}(E)$ that can be expressed by $2 \cdot F_0 \cdot F'_{Fe}(E) = 2 \cdot F_0 \cdot \alpha \cdot [f'[Fe^{3+}](E) - f'[Fe^{2+}](E)]$. Mulders *et al.* [22] do not determine F_0 and the α parameter separately. These parameters are determined by the charge sequence (α) and the lattice distortion (F_0). Instead, they fix the chemical shift (charge disproportionation) and fit the $\alpha \cdot F_0$ term. We note that a strong correlation exists between the chemical shift and the $\alpha \cdot F_0$ term. In fact, the charge disproportionation term can be written as $f'[Fe^{3+}](E) - f'[Fe^{2+}](E) = f'[Fe^{2.5+}](E + \Delta E/2) - f'[Fe^{2.5+}](E - \Delta E/2)$, ΔE being the chemical shift. When ΔE is small, this term can be approximated by $\frac{df'[Fe^{2.5+}](E)}{dE} \cdot \Delta E$. In this way, the same quality of the fit can be found with different

ΔE values if the product $\alpha \cdot F_0$ is a free parameter. Therefore, it is impossible to determine the value of this charge segregation without a quantitative analysis including the structure factor given by the exact CO sequence.

The crystal structure of $LuFe_2O_4$ distorts on cooling down from hexagonal $R\bar{3}m$ to monoclinic *C/2m* (phase I) and finally to triclinic $P\bar{1}$ (phase II). Only one crystallographic site is occupied by the Fe atoms in the $R\bar{3}m$ symmetry which splits into four different sites in *C2/m* and afterwards into six sites in $P\bar{1}$. We recall here that the non-resonant character of the (0, 0, *l*/2) reflections implies the lack of charge disproportionation between the Fe bilayers along the *c*-axis direction (*i.e.* anti-polar CO). This result is not compatible with a bimodal Fe valence distribution within the *C2/m* cell as derived from [20]. Since the multiplicity of Fe2 and Fe3 sites is twice the one of Fe1 and Fe4 sites, the charge disproportionation (δ) between Fe2 and Fe3 must be half of the one between Fe1 and Fe4, *i.e.* $\delta_{Fe1\text{-}Fe4} = 2\delta_{Fe2\text{-}Fe3}$. This means that the chemical shift between the distinct AASF corresponding to the different Fe sites must verify $\Delta E_{Fe1\text{-}Fe4} = 2\Delta E_{Fe2\text{-}Fe3}$. We have calculated the structure factor in the *C2/m* symmetry and the resulting general expressions for the intensity of the two kinds of resonant reflections are:

$$I_{\frac{1}{3}\frac{1}{3}l} \propto (F_{0,\frac{1}{3}\frac{1}{3}l})^2 + 2F_{0,\frac{1}{3}\frac{1}{3}l} N_{\frac{1}{3}\frac{1}{3}l} [(f'_{Fe1} - f'_{Fe4}) + (f'_{Fe2} - f'_{Fe3})] \quad (1)$$

$$I_{\frac{1}{3}\frac{1}{3}l} \propto (F_{0,\frac{1}{3}\frac{1}{3}l})^2 + 2F_{0,\frac{1}{3}\frac{1}{3}l} N_{\frac{1}{3}\frac{1}{3}l} [(f'_{Fe1} + f'_{Fe4}) - (f'_{Fe2} + f'_{Fe3})] \quad (2)$$

with $N_{hkl} = \Sigma_i \exp[2\pi(h'x_i + k'y_i + l'z_i)]$, being x_i, y_i and z_i the fractional coordinates of the Fe*i* (*i*=1,2,3,4) atoms and h',k',l' the Miller indices in the *C2/m* setting corresponding to the (1/3, 1/3, *l*/2) and (1/3, 1/3, *l*) indices in the hexagonal description. We note that the N_{hkl} factor is the same for the different Fe sites in *C2/m* and nearly equal for the three phases ($R\bar{3}m$, *C2/m* and $P\bar{1}$) since it is only determined by the atomic positions of the iron atoms that change very slightly among them.

Following from expressions (1) and (2), the proposed four-modal charge distribution successfully explains the occurrence of the (1/3, 1/3, *l*/2) reflections but fails to predict nonzero intensity for the (1/3, 1/3, *l*) reflections. Thus, this model qualitatively describes the absence of RXS intensity for the *l*=integer reflections between 320 and 240 K, but it cannot account for the coexistence of the two types of

resonant reflections below 240 K. We remember here that in the $P\bar{1}$ symmetry (phase II) there are six non-equivalent (*2i*) Fe sites in total. Taking into account the additional splitting of the monoclinic Fe2 and Fe3 sites into two sites denoted as Fe21,Fe22 and Fe31,Fe32 respectively, the general expression for the intensity of the (1/3, 1/3, *l*/2) and (1/3, 1/3, *l*) reflections are given by:

$$I_{\frac{1}{3}\frac{1}{3}\bar{l}} \propto (F_{0,\frac{1}{3}\frac{1}{3}\bar{l},})^2 + 2F_{0,\frac{1}{3}\frac{1}{3}\bar{l}}[N_{\frac{1}{3}\frac{1}{3}\bar{l}}{}^{a}(f'_{Fe1}-f'_{Fe4}) + N_{\frac{1}{3}\frac{1}{3}\bar{l}}{}^{b}(f'_{Fe21}-f'_{Fe32}) + N_{\frac{1}{3}\frac{1}{3}\bar{l}}{}^{c}(f'_{Fe22}-f'_{Fe31})]$$
$$I_{\frac{1}{3}\frac{1}{3}l} \propto (F_{0,\frac{1}{3}\frac{1}{3}l,})^2 + 2F_{0,\frac{1}{3}\frac{1}{3}l}[N_{\frac{1}{3}\frac{1}{3}l}{}^{a}(f'_{Fe1}+f'_{Fe4}) + N_{\frac{1}{3}\frac{1}{3}l}{}^{b}(f'_{Fe21}+f'_{Fe32}) + N_{\frac{1}{3}\frac{1}{3}l}{}^{c}(f'_{Fe22}+f'_{Fe31})] \quad (3)$$

where $N_{hkl}{}^{x}$ are the partial structure factors of each of the Fe sites.

This model explains the ocurrence of resonances of both (1/3, 1/3, *l*) and (1/3, 1/3, *l*/2) reflections. Since the (1/3, 1/3, *l*/2) reflections must remain almost unaltered between the two phases, the valence of Fe2(Fe3) would be the average of Fe21 and Fe22 (Fe31 and Fe32), so the charge disproportionation of Fe2 into Fe21 and Fe22 and Fe3 into Fe31 and Fe32 must be symmetric. Although there is a strictly six-modal valence distribution in phase II, we have assumed a simpler tri-modal valence distribution such as Fe21=Fe1, Fe31=Fe4 and Fe22=Fe32, which imposes the following relationships among the chemical shifts $\Delta E_{Fe1\text{-}Fe22}=\Delta E_{Fe22\text{-}Fe4}$ (i.e. $\Delta E_{Fe1\text{-}Fe4}=2\,\Delta E_{Fe22\text{-}Fe4}$).

We have fitted the energy-dependent RXS of the two series of (1/3, 1/3, *l*/2) and (1/3, 1/3, *l*) reflections using the two proposed models based on the four-modal and tri-modal valence distributions, respectively with only the chemical shifts, *i.e.* the charge disproportionations, as free parameters. The F_0 for each reflection has been estimated by comparison with permitted reflections and the sign has been obtained from the structural models. The real part of the Fe AASF, *f'*(*E*), has been obtained by the Kramers-Kronig transformation [31] from *f''*(*E*), deduced from the experimental x-ray absorption spectrum of $LuFe_2O_4$. This *f'*(*E*) corresponds to the average valence state +2.5 and has been used to simulate the contribution from each non-equivalent Fe site by shifting the energy scale following the empirical correlation between the chemical shift and the formal valence state (4 eV shift between Fe^{3+} and Fe^{2+}). Figure 3 illustrates the best fits for selected reflections of each family. We note that the same quality of the fit is obtained for the (1/3, 1/3, *l*/2) reflections using either of the two models because the average valence of Fe2 and Fe3 sites does not change. At the same time, the four-modal

distribution gives almost zero intensity for (1/3, 1/3, *l*) reflections. The fits yield the following results for the charge disproportionations: $\delta_{Fe1-Fe4}$ =0.54±0.05 e^- (and thus $\delta_{Fe2-Fe3}$ =0.27±0.05 e^-) in phase I whereas $\delta_{Fe1-Fe4}$ =0.60±0.05e^- ($\delta_{Fe22-Fe4}$=$\delta_{Fe1-Fe22}$=0.30±0.05 e^-) in phase II.

The combined HRPD and RXS studies have provided consistent results that clarify the so-called CO transition of $LuFe_2O_4$. Summarizing, $LuFe_2O_4$ suffers a first structural phase transition from $R\bar{3}m$ to *C/2m* symmetry on cooling at T_{CO}≈320 K. This transition is driven by the condensation of Y_2 modes that originate a split of the hexagonal iron site into four with different valence states resulting in the occurrence of (1/3, 1/3, *l*/2) reflections. The charge segregations obtained by the two techniques are very similar and demonstrate the absence of any bimodal charge distribution Fe^{2+}/Fe^{3+} and the lack of charge modulation along *c*-axis. Upon further cooling down, a second structural transition, coincident with the magnetic one at T_N≈240 K, takes place implying an additional decrease of the crystal symmetry to $P\bar{1}$ and new resonant (1/3, 1/3, *l*) superstructure reflections. In this case, some Γ_2^+ modes are the primary to yield the triclinic distortion resulting in a separation of the Fe atoms in six non-equivalent sites. The simplest model accounting for this additional charge modulation is a tri-modal valence distribution in which the six Fe valences can be grouped into three: one third of the iron atoms remain in the average 2.5 valence and the other two thirds segregate in valences 2.2 and 2.8. Figure 4 summarizes the successive sequence of charge disproportion on cooling: above T_{CO} the valence of the iron atoms fluctuates among the three valence states. In the *C2/m* phase, Fe1 and Fe4 choose a definite charge while Fe2 and Fe3 still fluctuate between two valence states, being their average charge disproportionation half of the Fe1-Fe4 disproportionation. Finally, in the $P\bar{1}$ phase below T_N the three different charges are localized.

This work, in agreement with previous studies [19,24], has demonstrated that neither the supposed ferroelectricity nor the Fe^{3+}/Fe^{2+} CO of $LuFe_2O_4$ are longer valid. Thus, it suggests reconsidering the recently proposed mechanism of electronic CO-based ferroelectricity.

The authors thank Diamond light source for granting beam time. Financial support from the Spanish MINECO (project nº MAT2012-38213-C02-01) and DGA (CAMRADS) is acknowledged.

References

[1] WANG K. F., LIU J. M. and REN Z. F., *Advances in Physics*, **58** (2009) 321.

[2] HILL N. A., *J. Phys. Chem. B* **104** (2000) 6694.

[3] VAN DEN BRINK J. and KHOMSKII D. I., *J. Phys.: Condens. Matter* **20** (2008) 434217.

[4] SUBIAS G. *et al., J. Synchr. Rad.* **19** (2012) 159

[5] SUBIAS G. *et al., J. of Phys. Conf. Series* **190** (2009) 012985

[6] GARCIA J. *et al., Phys. Rev. Lett.* **109** (2012) 107202

[7] IKEDA N. *et al., Nature* **436** (2005) 1136.

[8] KO K.-T. *et al., Phys. Rev. Lett.* **103** (2009) 207202.

[9] WEN J. S. *et al., Phys. Rev. Lett.* **98**, (2007) 246403.

[10] XIANG H.J. and WHANGBO M.-H., *Phys. Rev. Lett.* **98**, (2007) 246403.

[11] NAGANO A. *et al., Phys. Rev. Lett.* **99** (2007) 217202.

[12] ROUQUETTE J. *et al., Phys. Rev. Lett.* **105** (2010) 237203.

[13] MICHIUCHI T. *et al., Ferroelectrics* **378** (2009) 175.

[14] KUEPPER K. *et al., Phys. Rev. B* **80** (2009) 220409(R).

[15] WU W. *et al., Phys. Rev. Lett.* **101** 137203 (2008).

[16] DE GROOT J. *et al., Phys. Rev. Lett.* **108** (2012) 037206

[17] RUFF A. *et al., Eur. Phys. J. B* **85** (2012) 290

[18] NIERMANN D. *et al., Phys. Rev. Lett.* **109** (2012) 016405

[19] LAFUERZA S. et al., Phys. Rev. B **88** (2013) 085130

[20] DE GROOT J. *et al., Phys. Rev. Lett.* **108** (2012) 187601.

[21] BRESE N. E. and O´KEEFFEM, *Acta Crystallogr. Sect. B* **47** (1991) 192; BROWN I.D., The Chemical Bond in Inorganic Chemistry: The Bond Valence Model (Oxford University Press, Oxford, 2002).

[22] MULDERS A. M. *et al, Phys. Rev. Lett.* **103** (2009) 077602.

[23] BARTKOWIAK M. *et al., Phys. Rev . B* **86** (2012) 035121.

[24] LAFUERZA S. *et al., Phys. Rev. B* **89** (2014) 045129

[25] FITCH A. N., *J. Res. Natl. Inst. Stand. Technol.* **109** (2004) 133

[26] CAMPBELL B. J. *et al., J. Appl. Crystallogr.* **39** (2006) 607

[27] OROBENGOA D. *et al., J. Appl. Crystallogr.* **42** (2009) 820

[28] RODRIGUEZ-CARVAJAL J., *Physica B* **192** (1993) 55

[29] COLLINS S. P. *et al., AIP Conf. Proc.* **1234** (2010) 310

[30] ISOBE M. *et al., Acta Crystallographica C* **46** (1990) 1917

[31] TOLL J. S., *Phys. Rev.* **104** (1956)1760

Table 1: Refined lattice parameters, unit cell volume and refinement data for $LuFe_2O_4$ at 300 and 80 K. The reliability factors are defined in [28].

	350 K	**300 K**	**80 K**
Space group	$R\bar{3}m$	*C2/m*	$P\bar{1}$
a (Å)	3.4417(1)	5.9588(2)	5.9371(1)
b (Å)	3.4417(1)	10.3155(2)	5.9411(1)
c (Å)	25.2445(1)	16.9564(3)	16.9593(1)
α (°)	90	90	93.349(1)
β (°)	90	96.796(1)	93.298(1)
γ (°)	120	90	119.849(1)
Vol (Å^3)	258.971(1)	1034.954(4)	515.386(3)
Z	3	12	6
R_{Bragg} (%)	5.9	4.8	4.1

Figure Captions

Figure 1. Details of the high resolution powder diffraction patterns for $LuFe_2O_4$ at selected temperatures: (a) patterns at 400 K and 300 K emphasizing some of the superlattice peaks below T_{CO}≈320 K, this latter indexed in terms of the high temperature hexagonal cell $R\bar{3}m$ and (b) patterns at 300 K and 80 K showing the additional peak splitting below T_N≈240 K with peaks indexed in the *C2/m* and $P\bar{1}$ cells described in the text, respectively.

Figure 2. Temperature dependence of the integrated intensity in the I(θ) scans for selected superlattice reflections of the types (1/3, 1/3, *l*/2) *l* = odd and (1/3, 1/3, *l*) *l* = integer. Dashed lines indicate the charge ordering (T_{CO}≈320K) and magnetic (T_N≈240K) transition temperatures.

Figure 3. Experimental energy-dependent intensities at 17 K of representative (a) (1/3, 1/3, *l*/2) *l* = odd and (b) (1/3, 1/3, *l*) *l* = integer reflections through the Fe K-edge in the σ-σ' channel after being corrected for self-absorption (symbols). The best fits (solid lines) with the four-modal (red) and tri-modal (blue) Fe valence distributions as described in the text are also shown.

Figure 4. Multimodal valence distributions for the Fe atom in $LuFe_2O_4$ as deduced from the quantitative analysis of the structure factor, depicted on the monoclinic unit cell: (a) four-modal corresponding to the *C2/m* phase I and (b) tri-modal corresponding to the $P\bar{1}$ phase II.

Figure 1.

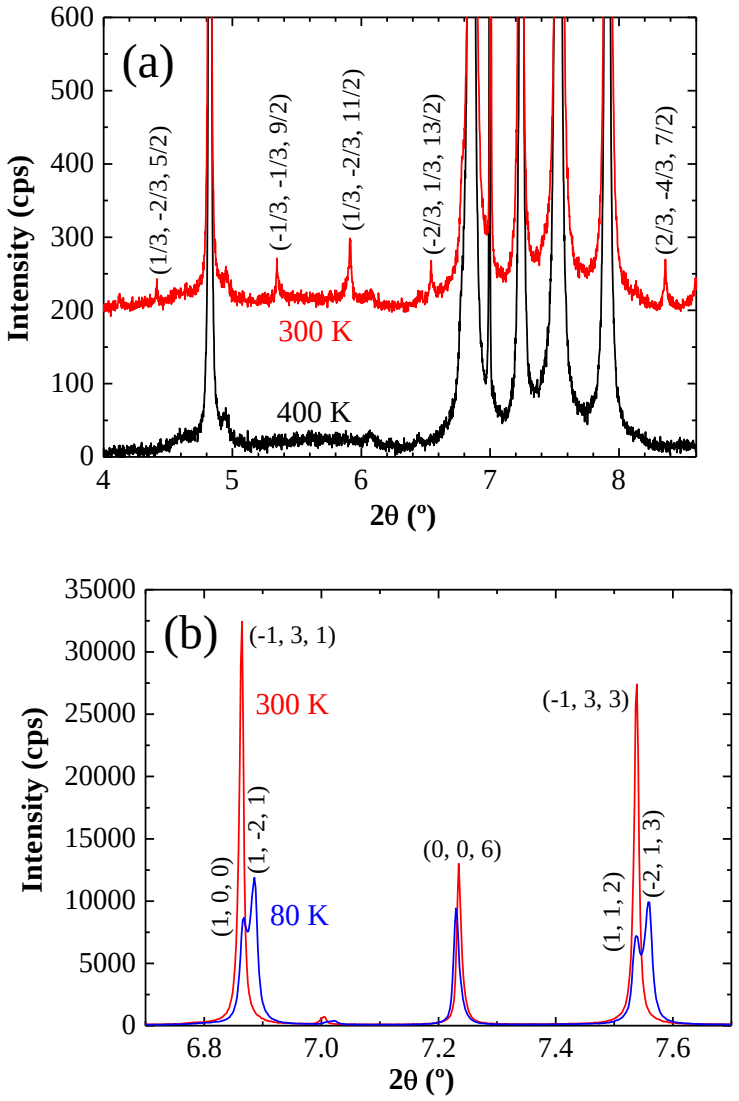

Figure 2.

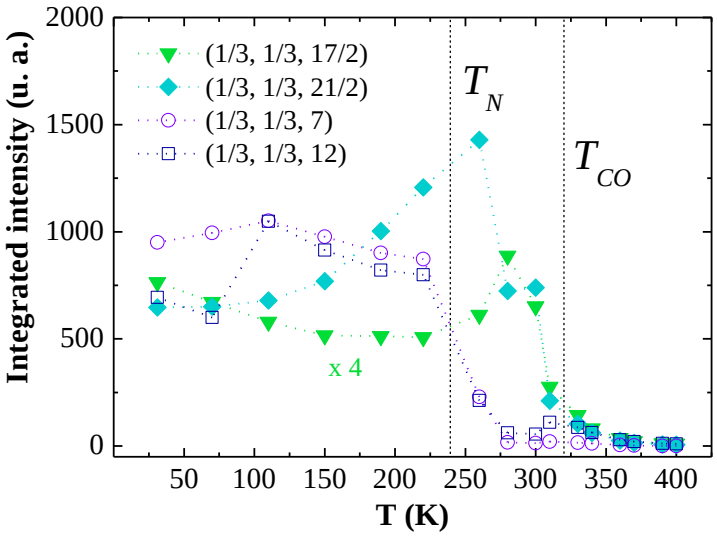
Integrated intensity (u. a.)
2000
1500
1000
500
0
50
100
150
200
250
300
350
400
T (K)
(1/3, 1/3, 17/2)
(1/3, 1/3, 21/2)
(1/3, 1/3, 7)
(1/3, 1/3, 12)
T_N
T_{CO}
x 4

Figure 3.

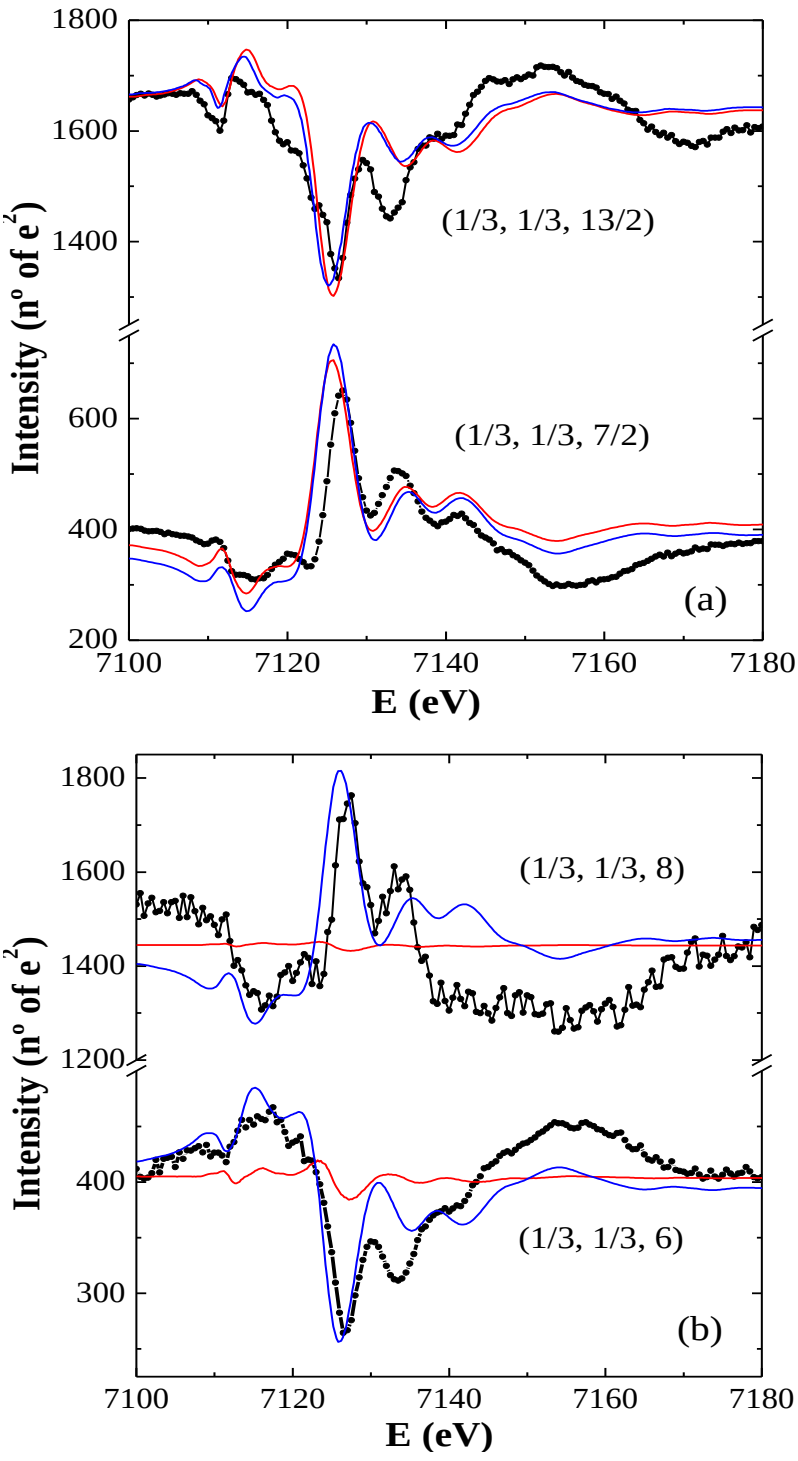
1800
1600
1400
600
400
200
(1/3, 1/3, 13/2)
(1/3, 1/3, 7/2)
(a)
Intensity (n° of e')
7100
7120
7140
7160
7180
E (eV)
1800
1600
1400
1200
400
300
(1/3, 1/3, 8)
(1/3, 1/3, 6)
(b)
Intensity (n° of e')
7100
7120
7140
7160
7180
E (eV)

Figure 4.

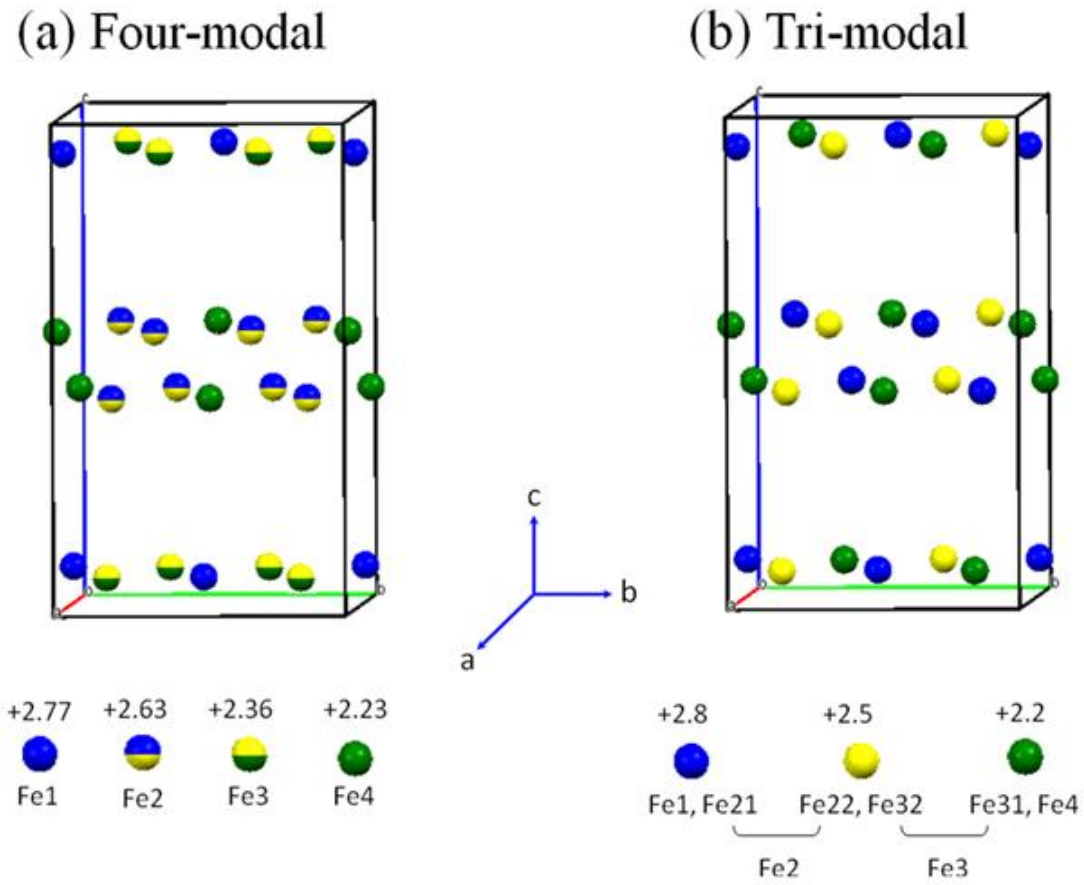
(a) Four-modal
(b) Tri-modal
c
b
a
+2.77
+2.63
+2.36
+2.23
Fe1
Fe2
Fe3
Fe4
+2.8
+2.5
+2.2
Fe1, Fe21
Fe22, Fe32
Fe31, Fe4
Fe2
Fe3